American Journal of Applied Sciences

Original Research Paper

The Impact of XRF-Escape on Energy Resolution of NaI: Tl Scintillation Detectors for Medical Imaging or Gamma-Ray Spectroscopy

[1]Raffaele Scafè, [2]Marco Puccini, [3]Rosanna Pellegrini and [1]Roberto Pani

[1]Department of Medico-Surgical Sciences and Biotechnologies, Sapienza University of Rome, Rome, Italy
[2]TERIN-ICT, ENEA-Italian National Agency for New Technologies, Energy and Sustainable Economic Development, Rome, Italy
[3]Department of Molecular Medicine, Sapienza University of Rome, Rome, Italy

Article history
Received: 08-12-2023
Revised: 25-03-2024
Accepted: 01-04-2024

Corresponding Author:
Raffaele Scafè
Department of Medico-Surgical Sciences and Biotechnologies, Sapienza University of Rome, Rome, Italy
Email: raffaele.scafe@gmail.com

Abstract: The effect of escape of X-ray fluorescence from scintillator elemental components on the detector energy resolution is investigated from a spectroscopic standpoint, for monolithic and pixelated crystals. Along with these, any other emissions in a given region of interest were also considered. In present spectral evaluations a range of ratios between the areas of the peaks (XRFesc) to (XRFesc + photoelectric) has been a priori set from 0-50%, according to literature indications, by 10% steps. At the upper extremes of these ratio values, maximum worsening in energy resolution values just below 40%, just above 10% and just below 10% have been estimated for the interest regions of Tc-99 and F-18e Cs-137, respectively. The inter-crystal XRF-escape is suggested to be considered among the effects producing image blurring in segmented scintillators due to the spread of events between neighbor pixels.

Keywords: Gamma-Ray Scintillation Detector, XRF-Escape, SPECT, PET, Inter-Crystal Interactions

Introduction

Robert Hofstadter presented in 1948 the NaI: Tl, a scintillator showing the highest light output up to this time by initiating the technique of pulse-height scintillation spectroscopy for gamma rays (Hofstadter, 1948). A "clear" single-crystal, coupled to a Photo-Multiplier Tube (PMT), gave much higher signals with respect to plastic scintillators, that, in turn, were sometimes used in the early practice. Due to the large preponderance of scattering events, compared to photo-electric ones, a pulse-height spectrum from plastics did not show a real photo-peak, but rather a Compton continuum. Consequently, the spectrum unfolding resulted in some laboriousness in order to obtain the energy value of primary gamma-rays.

Before Hofstadter, gamma-ray spectroscopy was performed by using experimental methods related to the range of gamma-ray energy, below or above 500 keV.

Above around 500 keV, the value of photon energy needed to be inferred from the distribution of secondary electrons emitted by atoms during the process of internal conversion, where the energy of the excited nucleus is transferred to the secondary particle to be emitted.

Taylor and Mott published in 1932 their theory of internal conversion of gamma-rays on the atomic orbitals, predicting the dependence of the value of conversion coefficient on both energy and multipolarity of the incident gamma-radiation for different atomic shells (Taylor and Mott, 1932).

Two years later, Jaeger and Hulme published their theory of internal conversion for gamma-rays above 1.022 MeV with the production of pairs of electron-positron for certain nuclei and found the dependence of the conversion coefficient on both energy and multipolarity of the radiation (Jaeger and Hulme, 1935).

According to these theories, an experimental technique was developed for charged particle detection, needing electrons focused by a transverse magnetic field and two Geiger-Müller counters operated in coincidence. The method showed (Latyshev, 1947) the major limitations of accurate beam focusing which, in the tour, needed a huge-activity radio-isotopic source (up to 20 GBq) and therefore, large and heavy shielding.

The reviews of modern physics published from 1940-1958 five issues of the tables of the Isotopes, under the supervision of G.T. Seaborg, collecting experimental quantities regarding both natural and artificial radio-isotopes (Livingood and Seaborg, 1940; Seaborg, 1944; Seaborg and Perlman, 1948; Hollander *et al*., 1953; Strominger *et al*., 1958). After 1948 the amount of contents in the issues has undergone strong growth due to worldwide dissemination of low-cost and portable NaI: Tl instrumentations, well suitable for measurements of low-activity samples. Edward U. Condon, editor of the last issue, in his preface, wrote: "This table is the 5th in a series of compilations which have appeared at approximately equal time intervals whose increasing length supplies a beautiful example of the exponential way in which knowledge grows." The trend has been reported in Fig. 1.

Thanks to the new detectors based on NaI: Tl and PMT, the development of knowledge in the field has had an exponential development. This is due to the substantial simplicity of the instruments, their good detection efficiency and their ease of use.

Spectrometric Background

In principle, in order to obtain quantitative results from a Single Photon Emission Computed Tomography (SPECT) investigation by using mono-energetic photons, it is mandatory to obtain the peak areas: (A) of the full energy produced by the primary radiation and, (b) of the escape peaks of XRF coming from the elemental scintillator components (Neiker and Bell, 1968). With such information, a quantitative analysis can be carried out independently of geometric shape, size and elemental composition.

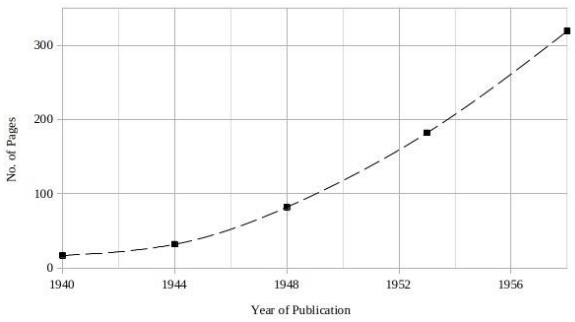

Fig. 1: Trend of growth of the number of pages per compilation of the tables of the Isotopes published in the reviews of modern physics in 1940, 1944, 1948, 1953 and 1958, respectively. This was produced by the massive use of the new NaI: Tl detectors made by the contributing researchers. The lengths of the collections were 17, 32, 82, 182 and 319 pages, respectively

Unfortunately, after about 75 years of continuous and almost absolute prevalence of the NaI: Tl in the field we are dealing with, it seems that we experimenters think that the changes in the response of a scintillator due to XRF-escape are limited roughly below 100 KeV of energy of the incident photons and that this can be corrected in the way suggested by Axel (1954).

But actually, in the case of SPECT investigations with Cr-51-labeled radiopharmaceuticals ($E\gamma$ = 320.1 keV), the escape peak is of small area because such gammas penetrate more and, consequently, the XRF from NaI: Tl are absorbed before escaping. The escape peak corresponding to this energy (E_{esc} = 320.1-29.2 = 290.9 keV), falls, by definition, on the leading edge of the photoelectric peak and is usually not distinguishable for reasons of NaI: Tl energy resolution at this energy. For this reason, evidently, the peak should be fitted to the sum of 2 Gaussians in order to be able to evaluate both areas of the escape and photoelectric peaks, respectively (Neiker and Bell, 1968, Fig. 12).

Often the area of the semi-peak above the centroid is even evaluated, but this neglects the contribution of the escape-peak.

It can also be assumed that the group of researchers who at the time proposed NaI: Tl for gamma-ray detection devoted much attention to changes in the spectrum at energies up to about 150 keV from the XRF escape process. In fact, around that energy, the emissions characterizing many fissile isotopes can be found, on which, as it is well known, the group was hardly working around the years 1940-50.

In that case, reasonably, a strong interest was focused on the methods to be applied in order to quantitatively investigate and also correct the gamma-ray spectra. In this sense, neglecting the K-XRF from sodium atoms because they are low in energy (<1 keV) as well as those from thallium, whose content in the mixture is in the order of a few units %, the choice of iodine as the main component seems the best trade-off between the need for good detection efficiency and that for quantitative interpretation of pulse-height spectra. By choosing iodine as a component, in fact, the XRF peaks come to fall at a position close to the minimum of the valley between Compton edge and 140 keV photoelectric peaks, where the area assessment is the most facilitated.

Unfortunately, the recent introduction of new scintillators based on mixtures of several elements characterized by Z up to 82, has greatly complicated the response of such compounds by multiplying the number of XRF-escape peaks on the left of photopeak.

Furthermore, Casey and Nutt (1986) proposed first a block detector made of an array of 32×8 BGO crystals to be explicitly used for Positron Emission Tomography (PET), each parallelepiped crystal sized 5.6×13.5×30 mm^3. It is to be noted that the crystal arrangement shows

relevant peripheral surface area where XRF photons can escape, from the array itself as well as from each primary single-crystal of the array.

Many efforts are continuing nowadays to study appropriate corrections for the Inter-Crystal Scattering (ICS) physical process. This phenomenon leads to the transfer of energy fractions of the primary photons to different locations in the crystal array, generating position-detecting errors of the respective events. A similar effect is to be expected in the case of XRF escape from the scintillator if such X-rays escape from the primary crystal of a block detector and are captured in one of the adjacent crystals.

The effect of such Inter-Crystal Escape (ICE) is to introduce a blurring of the PET image and is estimated to have a comparable impact (if not predominant) compared to ICS at least in the case of high-Z_{eff} scintillators (Indovina *et al*., 2022).

Beginning with the work of Casey and Nutt (1986), many authors have presented systems dedicated to studies on small animals based on scintillator arrays different from the BGO, including YAP: Ce (Di Domenico *et al*., 1998) and $Lu_{0.7}Y_{0.3}AP$: Ce (Kuntner *et al*., 2005) and on several devices for the readout of the scintillation light using PMTs o PSPMTs.

The contemporary wide development of new PSPMTs for light-spot detection is concisely described in Pani *et al*. (2019).

In principle, the process of X-ray escape does not occur in the case of a scintillation crystal with infinite size and with the gamma-ray source located inside it, because all the secondary radiation, resulting from the interactions, is absorbed in its volume. This contributes to collecting the entire energy of the incoming event, provided that all the scintillation light photons reach the photocathode (Knoll, 2010).

In real scale, certain cases, in which the atoms emitting the fluorescence X-rays are located in close proximity to an outermost wall of the scintillator, cannot contribute to the total event energy due to the escape of the fluorescence X-ray itself.

Such events tend to form other peaks, on the left of the full-energy one, at distances equal to the X-ray energies, being these X-rays characteristic of the scintillator components.

In principle, multiple escape peaks are created in the spectrum, depending on the number of components of the scintillator and on the atomic shells (K, L, M, …) involved in the processes.

In practice, for a NaI crystal, it is enough to consider, with a good approximation, the emissions from the iodine because the energy of the X-ray K-shell edge of sodium is around 1 keV only, against the 33 keV about of iodine (Table 1). This, substantially, makes the sodium K-escape peak practically indistinguishable from the full-energy peak.

Table 1: Elemental composition of the NaI scintillator and fluorescence K-shell edge X-ray energy

Element	Z (atomic number)	ECmp (fraction by weight)	K-shell edge (keV)
Na	11	0.153373	1.080
I	53	0.846627	33.168

In general, for all the elements of the table of Mendeleev, the atomic shells other than the K are characterized by both energies and intensities values strongly lower than the K-ones (Kaye, 1995), which authorizes us to disregard them.

The same occurs in the majority of cases for the doping elements added to the scintillator components for optimizing their light yield, at least in the cases where their content does not exceed a few percent.

Finally, since the standard deviation of the average X-ray energy of the K-shells of a given scintillator component is considerably small compared to the typical detector energy resolution, the energy values of the single shells of such a component can be replaced, in the calculation of the escape-peak position in the pulse-height spectrum by the respective mean values. The typical values of detector energy resolution, as a function of photon energy, are detailed in subsection 3.5.

Summarizing, for NaI, the iodine component will produce a specific escape-peak, on the left of the full-energy one, shifted from the last by a quantity equal to the average energy of the K-shells.

Last, it could be helpful to remark that the energy values of K X-rays are strongly increasing with respect to the atomic number Z of the considered individual scintillator component (Kaye, 1995). So, for each component, the higher the value of Z, the larger the shift on the left of the escape peaks from the full-energy ones.

Regarding the quantification of iodine X-ray escape from NaI, a former work deducing the correction factor of the photo-peak area for this process was presented (Axel, 1954). The method supposed that iodine X-rays were only from photoelectric interactions (i.e., their origin from Compton-scattered photons was excluded) and it was based on solid-angle calculations for front or lateral positions of a point-source with respect to a right-cylindrical scintillator. The importance of the correction was found dependent on the energy of the radiation, on the dimensions of the crystal and on the experimental setup. The order of magnitude of the ratio escape-to-total was found in the range from around 0.4-0.01 for photon energy ranging from 33-150 keV, respectively.

The same year an experimental work (Meyerhof and West, 1954) substantially confirmed Axel's results (Axel, 1954).

A scintillator figure-of-merit, called volumetric ratio, is introduced in the appendix, whose value characterizes a scintillation crystal, depending on geometric shape, elemental composition and mean-free path for a given photon energy value.

Materials and Methods

NaI Composition and Characteristic Fluorescence X-Rays

An evaluation of the impact of the X-ray escape process on the energy resolution of a NaI scintillation detector is given in the present work. For this purpose, we have considered the photon-energy range from 1 keV to 1 MeV, which includes the domain of interest for medical imaging with radionuclides, corresponding to the emissions of the most popular radiopharmaceuticals in use with techniques called SPECT and PET.

The values of the Elemental Composition (ECmp) of the NaI scintillator as well as the fluorescence K-shell edge X-ray energy are reported in Table 1. The ECmp values have been calculated at the NIST website (NIST, 2024), while the X-rays data are from (Kaye, 1995).

The characteristic fluorescence X-ray values from the NaI scintillator components and for the two innermost atomic shells are listed by ascending energy in Table 2. The X-ray data have been rearranged from (Kaye, 1995) and the calculated quantities are described in the respective column header. Intensity values have been estimated by using the approximation rules suggested in the same (Kaye, 1995). As it is well known, the intensity values are usually reported, shell by shell, relative to the most intense line for a given atomic shell. Lines whose energy values are below 1 keV have been omitted in the present evaluation.

NaI Interaction Data

The values of the interaction coefficients in the photon energy range from 1 keV to 1 MeV have been calculated at the NIST website by using the XCOM software and the photon cross sections database (NIST, 2024). Results are shown in Fig. 2.

The trend of the total linear interaction coefficient, as a function of the photon energy $\mu_{(E)}$, can be obtained, in the given photon-energy range, by summing the ones of the photoelectric and Compton curves because the other physical processes produce interactions only above the threshold of 1.022 MeV. The coherent scatter, which by definition is not an energy-spending physical process, is not added because it does not bring to the excitation of scintillator atoms. This can be written as in Eq. (1):

$$\mu_{(E)} = \tau_{(E)} + \sigma_{(E)} \quad (1)$$

where, $\mu_{(E)}$ represents the total linear interaction coefficient, while the $\tau_{(E)}$ *and* $\sigma_{(E)}$ stay for the photoelectric and Compton ones, respectively.

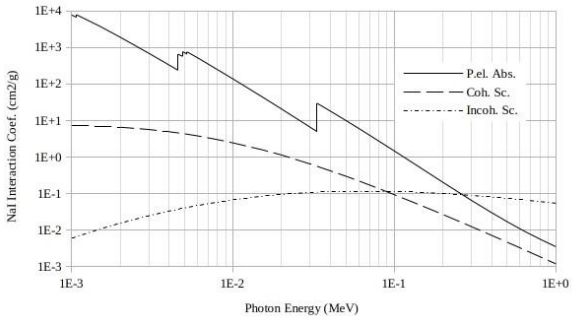

Fig. 2: Trends of the values of the interaction coefficients for the NaI scintillator, expressed in cm^2/g, as a function of the photon energy, based on data from (NIST, 2024). The discontinuities between 4 and 5 keV and from 30-40 keV refer to the L and K orbitals of the NaI components, respectively. It only affects, obviously, the photo-electric interaction

Table 2: Characteristic fluorescence X-rays (E≥1 keV) from the NaI scintillator components for the two innermost atomic shells and by ascending energy value and associate quantities

Element	Shell	Line identification	Energy (keV)	Weight = ECmp × intensity (keV)	Weighted average En. (keV)	Uncertainty (keV)
Na	K	Kα2	1.04	11.54	1.046	0.072
		Kβ3	1.07	2.30		
I	L	Ll	3.49	16.14	4.121	0.004
		Lα2	3.93	8.47		
		Lα1	3.94	76.20		
		Lβ1	4.22	84.66		
		Lβ4	4.26	16.93		
		Lβ3	4.31	28.84		
		Lβ2	4.51	5.03		
		Lγ1	4.80	5.29		
		Lγ3	5.07	4.23		
	K	Kα2	28.32	45.51	29.241	0.006
		Kα1	28.61	84.66		
		Kβ2	32.24	8.47		
		Kβ1	32.30	16.93		
		Kβ3	33.05	4.77		

By using the $\mu_{(E)}$ data, expressed in cm^{-1} with the density value of NaI of 3.67 g/cm^3 (Knoll, 2010), the corresponding value $\lambda_{(E)}$ of the Mean-Free-Path$_{(E)}$ ($MFP_{(E)}$) at the given photon energy, expressed in cm, can be obtained from Eq. (2) (Knoll, 2010):

$$\lambda_{(E)} = MFP_{(E)} = 1/\mu_{(E)} \quad (2)$$

Whose trend, as a function of the photon energy, is reported in Fig. 3.

The definition of this quantity by Knoll (2010) recalled from the same reference, is:

> *«the average distance traveled in the absorber before an interaction»*

As above mentioned, the events, whose interaction stories within the scintillators include an X-ray photon escaping from the detector, contribute to building a specific escape peak on the left of the full-energy peak, whose spread depends on the involved orbitals energy values. The distance (in energy units) between the centroids of these two peaks corresponds, respectively, to the energy of the fluorescence X-ray characteristic of the atom involved in the interaction.

Therefore one can write the Eqs. (3-4):

$$E_{Escape} = E_{Gamma} - E_{XRF} \quad (3)$$

where, of course:

$$E_{Gamma} \geq E_{XRFedge} \quad (4)$$

where the symbols represent the energy values as follows:

E_{Escape} : Escaping X-ray
E_{Gamma} : Incoming photon
E_{XRF} : X-ray fluorescence from a given atomic shell and
$E_{XRFedge}$: Edge of the given shell

Due to the substantial similarity of the values of the binding energies within a given atomic shell (Table 2), in an acceptable approximation for the present study, it is satisfactory to assume the E_{XRF} as the value of the average of the energies weighted by the respective intensity values for the atomic shells. Furthermore, given the difference between the average energy values for different atomic orbitals, it would be enough in the present evaluation to consider the K-orbital only.

The physical process of the X-ray escape is thus a threshold process, that is, it takes place when the value of the energy of the incident photon exceeds or at most equals that of the ionization energy of an electron that is bound to an atom of one of the scintillator components.

The discontinuities between 4 and 5 keV and from 30-40 keV, are shown in Figs. 2-3 and in Table 2, refer to the L and K orbitals, of the NaI components, respectively.

It should be observed that, in the given energy interval (1 keV-1 MeV) of the incident photon, the probability of interaction is distributed in a binary way, with a fraction between photo-electric and scattering coefficients dependent on the photon energy. The latter is, in turn, divided between elastic (or coherent, or also Rayleigh) and inelastic scattering (or incoherent, as well Compton) events. It is to be noted that the elastic scattering does not imply an exchange of energy between the incident photon and the atom involved in the interaction, but only a deviation of the trajectory of the photon itself from its original direction.

In this regard, see the Fig. 2 where the interaction probability trends are reported for the NaI scintillator. In particular, it can be noted that the elastic interaction is (variously) prevalent among the scattering events for photon energy up to 89 keV, while the photoelectric events are (largely) prevalent over the scattering events for energies below 286 keV.

Organic and Inorganic Scintillators

Regarding the process of X-ray escape, the behavior of organic and inorganic scintillators is in practice very different from each other because the formers typically have components with Z = *8* (oxygen) or less, while the latter do not show this limitation in *Z*.

Consequently, with reference to Eqs. (3-4), for the organic scintillators we have $E_{Escape} \approx E_{Gamma}$ since $E_{XRFedge} \leq 0.533$ *keV* (Kaye, 1995) and experimentally, only a minimally distorted single-peak is observed. In practice, these scintillators can be considered as escape-free.

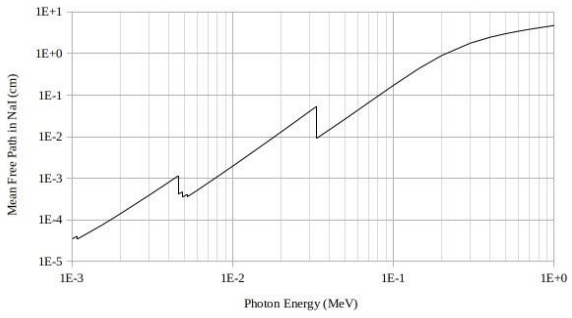

Fig. 3: Trend of the values of the mean-free path, expressed in cm, as a function of the photon energy for the NaI scintillator based on data from (NIST, 2024). The discontinuities between 4 and 5 keV and from 30-40 keV refer to the L and K orbitals, of the NaI components, respectively. It is in connection, obviously, with the photo-electric interaction

On the contrary, for the inorganics ones, it is usual to note a broadening of the peak in E_{Gamma} towards the left, up to its splitting, which depends on the scintillator elemental composition and on the value of E_{Gamma}. This can occur if one or more elements, with sufficiently high concentrations and with a high enough Z, are among the components of the scintillator. In fact, as the value of the $E_{XRFedge}$ increases versus Z at an average rate of about 1 keV per unit of Z (Kaye, 1995), its order of magnitude can become greater than the half-width at half-maximum of the peak in E_{Gamma} itself and this produces a splitting into two peaks.

Regions of Interest Definitions

The evaluation method is based on mathematical analysis tools and, particularly, Gaussian functions for representing the single-peaks and the gamma-ray spectrum in the Region of Interest (RoI) obtained by summing individual peaks.

For the calculation purposes, arranged by 2.5 keV photon-energy steps, two simplifying assumptions have been made:

1) The first one regards the detection efficiency, whose value affects the area of the peaks, that has been assumed constant within each selected RoI, due to their limited size with respect to the peak centroid value. Tables 3-5 report the values of the nuclear, of the atomic emissions, as well as of the iodine K-escape peaks calculated for each of them the average value and its standard deviation have been added to each table to quantify the overall dispersion
2) The second assumption refers to the iodine K-escape energy value that has been taken equal to the average of the single-shell energy value weighted by the respective intensity

In this regard, the following RoIs have been selected:

- 140 keV from the Tc-99 decay, the most diffuse isotope utilized as a radiotracer in the SPECT technique
- 511 keV from F-18 decay usually used in PET technique and
- 662 keV from Cs-137 decay, an isotope widely in use for calibration in gamma-ray spectroscopy

As specified in the respective "table of nuclear and atomic radiations from nuclear decay, in the Medical Internal Radiation Dose (MIRD) format from the Evaluated Nuclear Structure Data File (ENSDF)", the photons included in these RoIs are identified so as to include the emissions whose energy is close to the peak emission which is not distinguishable for energy resolution reasons. Data concerning the gamma emissions within the considered RoIs are reported in Tables 3-5.

Table 3: 140 keV RoI. Emissions from Tc-99 and the corresponding escape peaks are considered in the calculations. The values are reported in descending order. The half-life is 6.0072 H and the decay modes are β- (Kondev *et al*., 2021) and *IT* (NNDC, 2017)

(i)	Radiation(i)	E_{gamma}(i) (keV)	Yield(i) (Bq-s)$^{-1}$
1	γ 2	140.5	0.8890
2	Ce-L, γ 2	137.0	0.0106
3	Ce-K, γ 2	119.0	0.0879
4	γ 2 esc	111.3	
5	Ce-L, γ 2 esc	108.2	
6	Ce-K, γ 2 esc	90.2	
	Average	117.8	
	Std. deviation	19.0 (16%)	

Table 4: 511 keV RoI. Emissions from F-18 and the corresponding escape peak are considered in the calculations. The values are reported in descending order. The half-life is 109.77 min and the decay mode is ε (Kondev *et al*., 2021; NNDC, 2017)

(i)	Radiation(i)	E_{gamma}(i) (keV)	Yield(i) (Bq-s)$^{-1}$
1	γ ±	510.9	1.93
2	γ ± esc	481.7	
	Average	496.3	
	Semi difference	14.6 (3%)	

Table 5: 662 keV RoI. Emissions from 55-Cs-137 and the corresponding escape peaks are considered in the calculations. The values are reported in descending order. The half-life is 30.04 years and the decay mode is β^- (NNDC, 2017)

(i)	Radiation(i)	E_{gamma}(i) (keV)	Yield(i) (Bq-s)$^{-1}$
1	γ 2	661.7	0.8510
2	Ce-L, γ 2	655.7	0.0139
3	γ2 esc	632.5	
4	Ce-L γ2 esc	626.5	
5	Ce-K, γ 2	624.2	0.0766
6	Ce-K γ2 esc	595.0	
	Average	632.6	
	Std. deviation	24.1 (3.8%)	

Peaks Representation

Each peak, relating to the gamma photons emitted by the given radioisotopic source within the assigned RoI, was represented by using a Gaussian function centered at the photon energy E_{gamma} as described in Eq. (5):

$$Counts_{(E)} = Yield_{(E)} \times Exp\left(k \times \left(E - E_{gamma}\right) / FWHM_{(E)}^{\ 2}\right) \quad (5)$$

where, both $Yield_{(E)}$ and E_{gamma} are from the appropriate table among Tables 3-5, while the multiplicative constant k at the exponent is $k = -4 \times Ln(2) \approx 2{,}773$ and $FWHM_{(E)}$ is calculated by using the Eqs. (6) and (9) describe, for a typical NaI: Tl detector, the linear decreasing trend of the natural logarithm of the energy resolution as a function of the natural logarithm of the photon energy expressed in units of $m_0 c^2$:

$$Ln\,R\;=\;a\times Ln\left(\;E\;/\;m_0c^2\right)\;+\;b \tag{6}$$

where, m_0 is the value of the rest mass of the electron, c is the value of the speed of light in the vacuum and a and b are parameters assuming the values of the Eq. (7) which have been obtained from the Knoll (2010), Figs. 10-17:

$$a\;=\;-\;0.4332\;\text{and}\;b\;=\;-\;1.9774 \tag{7}$$

Once the value of LnR for the given energy has been obtained, the value of R is calculated by using the Eq. (8):

$$R=Exp\left(Ln\;R\right)=\Delta E\;\;/\;\;E \tag{8}$$

From which one can derive the value of the spread at half height ΔE by using Eq. (9) for the energy of the considered emission:

$$FWHM\left(E\right)=\Delta E=R\times E \tag{9}$$

From the total peaks (Figs. 4-6) one can obtain the values of the spreads at half-height and the peak positions, giving the corresponding values of energy resolution as defined by Eq. (8).

Energy Resolution Trends

The energy resolution trends of NaI: Tl for the selected RoIs, can be evaluated by using a priori assumptions for the values of the ratio of the areas of the peaks (XRFesc) to (XRFesc + photoelectric) that ranges, by definition, from 0-100% for no escape (i.e.,): Ideal infinite detector) and for total escape (i.e.,): Detector with thickness tending to zero), respectively. In the present evaluations, the a priori range has been set to the interval from 0-50%, by 10% steps, also based on what was reported in (Axel, 1954).

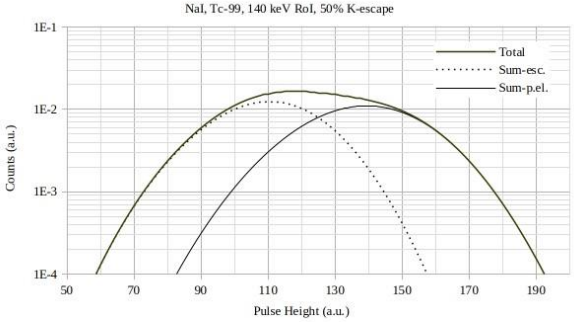

Fig. 4: Tc-99: NaI: Tl calculated sum-photo-electric and iodine-K sum-escape peaks in the 140 keV RoI, showing the enlargement on the left of the maximum of the Total curve due to the contribution of all the emissions and of respective iodine-K XRF-escape emissions, assumed at 50% of the total. The semi-log diagrams are referenced in the legend, from top to bottom, in the same sequence as the curves themselves. The Tc-99 emissions are detailed in Table 3

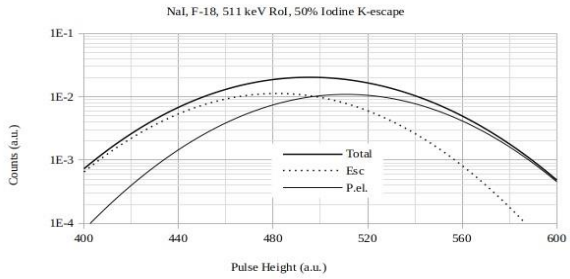

Fig. 5: F-18: NaI: Tl calculated photo-electric and escape peak in the 511 keV RoI, showing the enlargement on the left of the maximum of the total curve due to the contribution of the iodine-K XRF-escape emissions, assumed at 50% of the total. The semi-log diagrams are referenced in the legend, from top to bottom, in the same sequence as the curves themselves. The F-18 emissions are detailed in Table 4

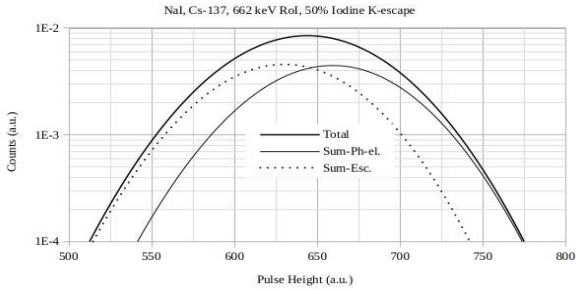

Fig. 6: Cs-137: NaI: Tl calculated sum-photo-electric and iodine-K sum-escape peaks in the 662 keV RoI, showing the enlargement on the left of the maximum of the total curve, due to the contribution of respective iodine-K XRF-escape emissions, assumed at 50% of total. The semi-log diagrams are referenced in the legend, from top to bottom, in the same sequence as the curves themselves. The Cs-137 emissions are detailed in Table 5

It is important to remark that each RoI includes not only the main source emission but also other nuclear emissions, falling in the RoI itself, due to different radio-tracer decay modes (Tables 4-5). This observation is important not only from the spectrometric point of view but also from that of Monte Carlo simulations. In fact, in almost all cases, in addition to the usual rejection of the effects of the XRF escape, the secondary emissions belonging to the RoI are also neglected, limiting the interest to the cases of monoenergetic gamma-ray sources. This makes the simulation results of little significance, for the part that estimates the energy resolution of an assembly in a given RoI.

On these bases, each gamma emission of the RoI having a significative yield, is described in the present work by a Gaussian curve centered at the given energy. An energy detail of 2.5 keV/channel is adopted. When the RoI cases are completed (Tables 4-5), the Total curve is calculated by summing, channel by channel, the values of all RoI's own trends.

The following should be noted for such curves. The first element consists in the structural asymmetry of the Total peaks since, by construction, they are obtained as sums of curves characterized by different centroids (and peak values), all located at lower energies than the photoelectric peak.

The second element to keep in mind is that the observed pulse-height spectra, seem not suitable for representation by a single Gaussian, because each of them represents a different physical process.

A third element to consider is that, among the contributions that may occur in a pulse-height spectrum, there may be others, not discussed here, such as sum peaks that affect instead the descending part of the Total peak (Knoll, 2010).

As a final methodological observation, the reader is asked to note that, in the concrete case of designing a specific detector block, the approach described in the present work cannot exclude the necessary Monte Carlo simulations to study device response. However this can be advantageously done only after the basic elements, such as the elemental composition of the scintillator, its size and geometric shape, have been identified. Indeed, as can be guessed, it is not convenient to proceed with ab initio logic, which would require substantial computational resources to reach design conclusions that conversely can be obtained by means of physics considerations such as those proposed in this study.

Results and Discussion

Figures 4-6 show the responses of a NaI: Tl scintillator for the emissions in the RoIs reported in Tables 3-5. For illustrative purposes, the iodine-K XRF escape emissions have been assumed at 50% of the total.

The calculation results, shown from here on, have been repeated with values of percent of escape varying in the range between 0 (no escape) and 50% of (escape + photoel.), by 10% steps. The results of these evaluations are reported in the Figs. 7-10. The escape-percent values assumed in these evaluations may appear excessive, but nevertheless a NaI: Tl detector can be thought of in both monolithic or pixelated form, whose dimension along the z-axis (usually referred to as thickness) can vary in real cases from a few millimeters to some inches. The ranges of thickness variability therefore include the so-called thin crystals, the use of which is sometimes preferred in cases of need for optimized energy resolution. Pixelated structures are expressly considered with reference to the PET detection blocks (Casey and Nutt, 1986).

But it is quite clear that the definition of a thin crystal can only refer to the definition of MFP (Knoll, 2010) which, as illustrated in Fig. 3 for the NaI: Tl, varies considerably as a function of the photon energy, also showing the discontinuities clearly visible in the Fig. 3 itself.

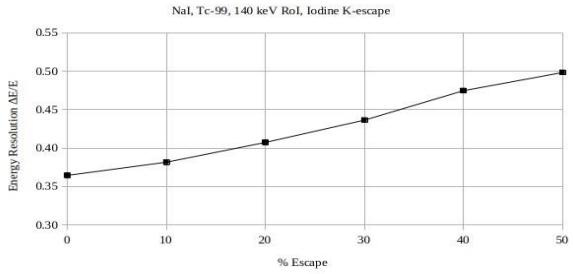

Fig. 7: Tc-99: NaI: Tl calculated energy resolution trend for the 140 keV RoI and iodine-K XRF escape-to-(escape + photoel) ratio in the range from 0-50%

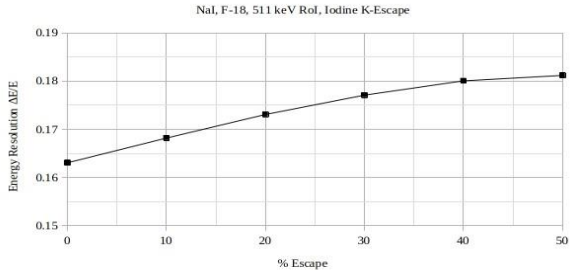

Fig. 8: F-18: NaI: Tl calculated energy resolution trend for the 511 keV RoI and iodine-K XRF escape-to-(escape + photoel) ratio in the range from 0-50%

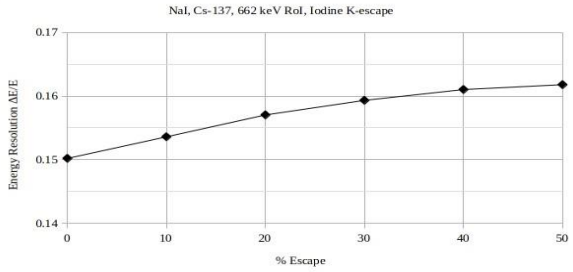

Fig. 9: Cs-137: NaI: Tl calculated energy resolution trend for the 662 keV RoI and iodine-K XRF escape-to-(escape + photoel) ratio in the range from 0-50%

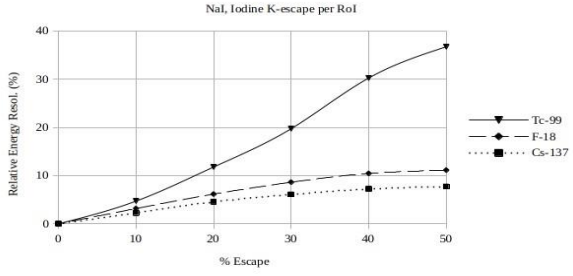

Fig. 10: NaI: Tl: Comparison of the calculated percent energy resolution trends for the respective energy RoIs, as a function of the percent of the iodine-K XRF escape with respect to (escape + photoel). The RoIs are shown in the legend from top to bottom in the same sequence as the curves

As could have been expected from the observation and the inter-comparison of Tables 3-5, among the given RoIs, the one most sensitive to the effects of the shifting of the peaks is at 140 keV which shows, moreover, the highest dispersion of the average referred to the average itself (16%).

Among the given RoIs, the 511 keV one is the "cleanest" since, in addition to the β + annihilation, it only shows the additional contribution from the X-ray escape (3% around).

On the other hand, the case of RoI at 662 keV, while showing a high absolute value of the dispersion of the mean, nevertheless shows a higher mean value which produces a smaller relative dispersion (3.9%).

The graphs shown in the Figs. 7-9 consistently show an increasing trend of the energy resolution $\Delta E/E$, starting from the respective initial energy-dependent value of each RoI. This is justified, on the one hand, by the widening effect due to the overlapping of the escape peaks to the ones corresponding to the emissions and, on the other hand, by the contribution of the rest of the emission (s) present in the RoI.

Moving on to the values expressed in percent, the final plot of Fig. 10 shows the worsening in energy resolution for the different RoIs, which results in an amplified increase the more the escape percentage of the iodine-K X-ray increases, particularly for the lowest-energy RoI.

Conclusion

Traditionally, attention is paid to the physical process of escape of fluorescence X-rays when one has to deal with thin NaI: Tl monolithic crystals coupled to a single-channel PMT for low-energy spectroscopy. But an accumulation of events in the pulse-height spectrum, on the left of the photopeak, at a distance equal to the iodine K-shell X-rays energy, takes always place. In fact, there is no physical reason inhibiting the process of X-ray escape, making it visible in an enhanced way only in particular conditions.

Understanding that a Monte Carlo experiment is the most reliable way to do these evaluations, however, some basic information can be preliminarily evaluated as discussed in the present work.

The impact of the X-ray escape process on the energy resolution of a scintillation detector for gamma-ray spectroscopy is shown in the plots of Figs. 4-6, drawn for values of escape-to-(escape + photoel.) ratio from 0-50%. Even in cases of lower impact, it is always possible to detect the presence of escape by simply evaluating the derivative of the count curve with respect to the channel number to highlight its points of relative minimum, inflection, or maximum.

For pixelated crystals as well as for thin monolithic ones, a noticeable number of cases occur in which the atoms releasing the fluorescence X-rays are located in close proximity to an outer wall of the scintillator and the contribution to the full-energy peak of the X-rays itself can be lost.

The quantity V_{ratio}, defined as the ratio of the volume of the outermost layer to the total scintillator volume, being the thicknesses of such layer equal to the $MFP_{(E)}$ has been evaluated in the Appendix. By construction, from that layer, on average, the fluorescence X-ray has a probability of escaping.

In medical imaging, this makes the escape process an important potential image-blurring factor, because of its numerical competing (or even dominating) effect, compared to inter-pixel scattering, to the point that it would be appropriate to speak of inter-pixel escape effect spreading events between the primary pixel and the first neighbors' ones, only.

This emphasizes, once again, the advantage of recognizing multi-pixel interactions also when X-ray escape occurs because, in this case, the event energy is spread in more than one pixel bordering the primary one.

In turn, this makes the prediction of the fraction of escaping fluorescence X-rays as a function of the scintillator elemental composition, as well as of the pixel size one of the most important tools to have on hand when designing a high-resolution pixelated detector, because of the possibility of recognizing and discarding the events undergoing multi-pixel interactions (Indovina *et al*., 2022).

Future work will be dedicated to evaluating the properties of scintillators from a specific spectroscopic point of view, especially the role of fluorescence X-ray escape. In particular, the spectrometric consequences of their elemental composition will be focused paying special attention to the presence of XRF components in regions of the pulse-height spectrum where the corresponding XRF peaks are very difficult to evaluate, like over the Compton-response regions, making corrections very difficult to perform.

Future works will be aimed to show the so-called XRF footprint, evaluated for a number of scintillators developed ab initio up today, with the ambitious full intention of producing a true "XRF atlas of scintillators".

Acknowledgment

- This research did not receive any specific grant from funding agencies in the public, commercial, or not-for-profit sectors
- Publication ethics individual contributes
  Raffaele scafè: Drafting the manuscript for significant intellectual content

Marco puccini: Data analysis and written of the manuscript
Rosanna pellegrini: Organization and final approval; Roberto pani: Conception and final approval

- The corresponding author affirms that all of the other authors have read and approved of the manuscript
- The authors affirm: <<the manuscript has been prepared in accordance with "science publication's journals instructions to authors" and the content of this manuscript, or a major portion thereof, has not been published in a referred journal nor being submitted for publication elsewhere.>>
- Authorship: Authors approve the manuscript as has been submitted to AJAS for publication

Funding Information

The authors have not received any financial support or funding to report.

Author's Contributions

Raffaele Scafè: Drafted the manuscript for significant intellectual content.

Marco Puccini: Data analysis and written of the manuscript.

Rosanna Pellegrini: Organization and final approval.

Roberto Pani: Conception and final approval.

Ethics

This article is original and contains unpublished material. The corresponding author confirms that all of the other authors have read and approved the manuscript and no ethical issues involved.

References

Axel, P. (1954). Intensity Corrections for Iodine X-Rays Escaping from Sodium Iodide Scintillation Crystals. *Review of Scientific Instruments*, *25*(4), 391. https://doi.org/10.1063/1.1771073

Borrazzo, C., Bettiol, M., Bennati, P., Preziosi, E., Fabbri, A., Scafe, R., Pellegrini, R., & Pani, R. (2016). Monte Carlo Simulation to Evaluate Factors Affecting Imaging Performances of Compact Scintillation Gamma Camera. *IEEE Xplore*, 1-5. https://doi.org/10.1109/nssmic.2016.8069537

Casey, M. E., & Nutt, R. (1986). A Multicrystal Two Dimensional BGO Detector System for Positron Emission Tomography. *IEEE Xplore*, *33*(1), 460-463. https://doi.org/10.1109/tns.1986.4337143

Di Domenico, G., Scandola, M., & Zavattini, G. (1998). YAP-PET: First Results of a Small Animal Positron Emission Tomograph Based on YAP: Ce Finger Crystals. *IEEE Xplore*, *45*(6), 3105-3108. https://doi.org/10.1109/23.737671

Hofstadter, R. (1948). Alkali Halide Scintillation Counters. *Physical Review*, *74*(1), 100. https://doi.org/10.1103/physrev.74.100

Hollander, J. M., Perlman, I., & Seaborg, G. T. (1953). Table of Isotopes. *Reviews of Modern Physics*, *25*(2), 469-651. https://doi.org/10.1103/revmodphys.25.469

Indovina, L., Scafè, R., Puccini, M., Pellegrini, R., & Pani, R. (2022). A new Generation of Scintillation Detectors with Identification of Events Undergoing Multiple Interactions for Gamma-Ray Imaging and Spectroscopy. *Applied Radiation and Isotopes*, *184*, 110189. https://doi.org/10.1016/j.apradiso.2022.110189

Jaeger, J. C., & Hulme, H. R. (1935). The Internal Conversion of γ-rays with the Production of Electrons And Positrons. *Proceedings of the Royal Society of London*, *148*(865), 708-728. https://doi.org/10.1098/rspa.1935.0043

Kaye, G. W. C. (1995). *Kaye and Laby-Tables of Physical and Chemical Constants* (National Physical Laboratory.,). Middlessex.

Knoll, G. F. (2010). *Radiation Detection and Measurement* (4th Ed.,). John Wiley & Sons.

Kondev, F. G., Wang, M., Huang, W. J., Naimi, S., & Audi, G. (2021). The NUBASE2020 Evaluation of Nuclear Physics Properties. *Chinese Physics C*, *45*(3), 030001. https://doi.org/10.1088/1674-1137/abddae

Kuntner, C., Auffray, E., Bellotto, D., Dujardin, C., Grumbach, N., Kamenskikh, I. A., Lecoq, P., Mojzisova, H., Pedrini, C., & Schneegans, M. (2005). Advances in the Scintillation Performance of LuYAP:Ce Single Crystals. *Nuclear Instruments and Methods in Physics Research Section A: Accelerators, Spectrometers, Detectors and Associated Equipment*, *537*(1-2), 295-301. https://doi.org/10.1016/j.nima.2004.08.030

Latyshev, G. D. (1947). The Interaction of γ -Rays With Matter and the Spectroscopy of γ -Radiation. *Reviews of Modern Physics*, *19*(2), 132-145. https://doi.org/10.1103/RevModPhys.19.132

Livingood, J. J., & Seaborg, G. T. (1940). A Table of Induced Radioactivities. *Reviews of Modern Physics*, *12*(1), 30-46. https://doi.org/10.1103/RevModPhys.12.30

Meyerhof, W. E., & West, H. I. (1954). Note on the Escape Peak Correction for NaI(Tl) Crystals. *Review of Scientific Instruments*, *25*(10), 1025. https://doi.org/10.1063/1.1770905

Neiker, J. H., & Bell, P. R. (1968). V - The Scintillation Method. In K. Siegbahn (Ed.), *Alpha-, Beta- and Gamma-Ray Spectroscopy* (1-, pp. 245-302). Elsevier. https://doi.org/10.1016/b978-0-7204-0083-0.50010-9

NIST. (2024). *XCOM: Photon Cross Sections Database*. Website. https://psrc.aapt.org/items/detail.cfm?ID=262

NNDC. (2017). Nuclear Decay Data in the MIRD Format. *National Nuclear Data Center*. https://www.nndc.bnl.gov/nudat3/mird/

Pani, R., Guidoccio, F., Scafè, R., Zanzonico, P., & Mariani, G. (2019). General-Purpose Gamma Cameras, Dedicated Gamma Cameras and Gamma-Probes for Radioguided Surgery. *In Springer Link* (1st Ed., pp. 137-171). Springer, Cham. https://doi.org/10.1007/978-3-319-95564-3_6

Pani, R., Pellegrini, R., Cinti, M. N., Longo, M., Donnarumma, R., D'Alessio, A., Borrazzo, C., Pergola, A., Ridolfi, S., & Vincentis, G. D. (2016). Development of a Novel Gamma Probe for Detecting Radiation Direction. *Journal of Instrumentation*, *11*(01), C01002. https://doi.org/10.1088/1748-0221/11/01/c01002

Seaborg, G. T. (1944). Table of Isotopes. *Modern Physics*, *16*(1), 1-32. https://doi.org/10.1103/RevModPhys.16.1

Seaborg, G. T., & Perlman, I. (1948). Table of Isotopes. *Reviews of Modern Physics*, *20*(4), 585-667. https://doi.org/10.1103/RevModPhys.20.585

Strominger, D., Hollander, J. M., & Seaborg, G. T. (1958). Table of Isotopes. *Reviews of Modern Physics*, *30*(2), 585-904. https://doi.org/10.1103/revmodphys.30.585

Taylor, H. M., & Mott, N. F. (1932). A Theory of the Internal Conversion of γ-rays. *Proceedings of the Royal Society A*, *138*(836), 665-695. https://doi.org/10.1098/rspa.1932.0209

Appendix-Volumetric Ratio

Understanding that a Monte Carlo experiment is the most reliable way to do this evaluation, however, some information can be roughly evaluated as discussed in the following.

Figure 11 shows the portions of a crystal, close to its walls, from which the fluorescence X-rays from a scintillator component have a chance of escaping from the crystal. The cases of the cylindrical and parallelepiped shapes are depicted at the top and at the bottom of Fig. 11, respectively, both considered in the present evaluation.

The photons from the most popular nuclear medicine radio-tracers travel in NaI for $MFP_{(E)}$ ranging from around 0.4 up to 3.0 cm and reach the value of around 4.0 cm for the 661.7 keV photons from the Cs-137 main emission.

On the other hand, the $MFP_{(E)}$ values for K-shell X-rays from NaI components are around 3.439×10^{-5} and 9.122×10^{-3} cm from sodium and iodine, respectively. As a consequence, the escape process of these X-rays concerns the atoms that make up the outermost layer of all the faces of the scintillator (Fig. 11), having this layer the thicknesses just above reported from sodium and iodine, respectively. Furthermore, the atomic emissions follow an isotropic spatial distribution and only the X-rays moving towards the crystal walls have a chance of escape from the crystal itself without depositing their energy in the scintillator.

The interaction probability within a generic absorber for a parallel beam of mono-energetic gamma-rays is expressed by the well-known Eq. (10):

$$\left(Io-I\right) \ / \ Io=1 - Exp(-\mu_{(E)}x) \tag{10}$$

where, Io and I represent the beam intensities in or out of the absorber, respectively; $\mu_{(E)}$ stays, according to Eq. (1), for the total linear interaction coefficient of the absorber at the given energy and x represents the thickness traveled in the absorber.

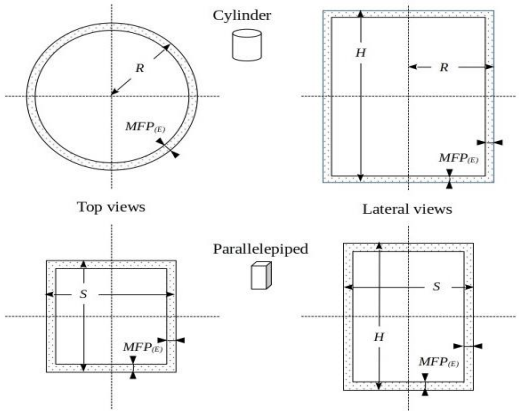

Fig. 11: On average, to successfully escape from the crystal, an X-ray must not only be emitted from one of the dotted regions of NaI close to the walls but the X-ray itself must also be oriented outward. It should be noted also that the $MFP_{(E)}$ depends on the atomic number Z of the emitting atom, i.e., sodium or iodine, respectively, whose values are reported in Table 2. Thus, the drawing is not to scale

By setting $x = MFP_{(E)}$ in Eq. (10), one can verify that the beam intensity interacting within the absorber, relative to the incoming value, assumes a value of around 0.632.

Equation (11) defines the quantity V_{ratio} as the ratio of the volume of the outermost layer to the total scintillator volume, being the thicknesses of such layer equal to the $MFP_{(E)}$, from which the fluorescence X-ray has a probability of escaping:

$$V_{ratio} = V_{layer} \ / V_{scint} \tag{11}$$

where:

V_{ratio} = Volumetric ratio

V_{layer} = Volume of the outermost layer whose thickness is $MFP_{(E)}$ and
V_{scint} = Total volume of the scintillator

As the sketch of Fig. 11 shows, in a first approximation, the fraction of escaping X-rays can be intuitively assumed to be proportional to the value of V_{ratio} shown by the given crystal, because the higher this value, the higher the escape-peak area in the gamma-ray spectrum.

A second estimation can be taken for the thickness of this layer that can be attributed to iodine only, due to their much higher intensity compared to sodium, whose atomic number *Z*, in turn, is much lower (Table 1).

With reference to the considerations about the escape process reported in Knoll (2010):

> *«These peaks are generally labeled "X-ray escape peaks" and tend to be most prominent at low incident gamma-ray energies and for detectors whose surface-to-volume ratio is large»*

The second assertion has suggested the study on the V_{ratio} parameter, which takes into account both the shape of the scintillator and its elemental composition.

To this aim, it is convenient to make a distinction related to the shape and to the geometry of the scintillation crystal.

Monolithic and Pixelated Scintillation Crystals and Readout Setup

Even if the scintillation crystals can be arranged with the shapes and the segmentation types more adequate to the specific application, the evaluations are hereafter limited to the cases of:

1) A right-cylindrical scintillator, coupled to a single-channel PMT
2) A square array of right-parallelepiped crystal pixels with a square-base, coupled to a multi-anode PSPMT

Case 1 works in pulse-height modality, like in (Knoll, 2010), while case 2. is operated in charge-spread mode (Indovina *et al*., 2022) that allows recognizing (and discarding) the events undergoing multi-pixel interactions within the array.

Right-Cylindrical Scintillation Crystal with Single-Channel PMT

To evaluate Eq. (11) for a right-cylindrical scintillator one can write Eq. (12):

$$V_{scint} = \pi \times R^2 \times H \tag{12}$$

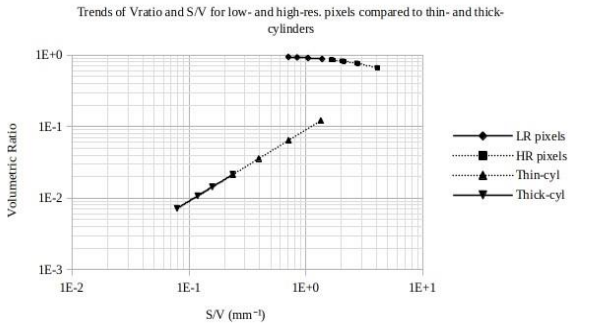

Fig. 12: Comparison of the trends of V_{ratio} for the iodine-K X-rays from NaI as a function of the *S/V* for both the pixelated-parallelepiped-top and the monolithic-cylindrical-crystals (bottom). As one can note, the *S/V* ratio parameter seems to fail to take into account the differences in the size, in their shape, as well as in the elemental composition of the scintillator itself. On the other hand, the parallelepiped crystals (upper curve) show a more marked tendency to favor the X-ray escape in comparison with the cylindrical ones (lower curve)

where, *R* and *H* are the values of lengths of radius and height of the cylinder, respectively.

Consequently, for the V_{layer} value, the Eq. (12) can be written like in Eq. (13):

$$V_{layer} = V_{scint} - \pi \times (R - MFP_{(E)})^2 \times (H - MFP_{(E)}) \tag{13}$$

In which the value of the interaction probability is around 0.632.

Regarding the monolithic cylindrical scintillation crystals, standard-sized 1×1, 2×2 and 3×3 inch, usually utilized for spectroscopic general-purpose have been investigated in the present study. In addition to these, also the 2-inch in diameter with height decreasing from 1-inch down to 0.0625-inch (about 1.6 mm), used for high-resolution small-field-of-view medical imaging, have been included. The results of evaluations for all these crystals are reported in Fig. 12, where the standard-sized crystals and the smaller ones are referred to as “thick cyl” and “thin cyl”, respectively.

Square-Array of Right-Parallelepiped Crystal-Pixels with PSPMT

Even if NaI does not represent the ideal material for assembling an array of crystal-pixel due to its tendency to fracture under fast changes of temperature, however, pixels made of that material have been included in the present study because NaI is the gold standard for gamma-ray spectroscopy. As a consequence of a fracture in a pixel, the transport of luminous photons along its axis is strongly compromised by their reflections back at the fractures itself, resulting in a dramatic decrease in the

light output at the pixel light-output-face up to making the event undetectable.

To evaluate Eq. (11) for a right-parallelepiped pixel one can write Eq. (14):

$$V_{scint} = S^2 \times H \tag{14}$$

where, *S* and Hare are the lengths of the pixel-side and of pixel height, respectively.

Consequently, for the V_{layer} value, the Eq. (15) can be written:

$$V_{layer} = V_{scint} - (S - MFP_{(E)})^2 \times \left(H - MFP_{(E)}\right) \tag{15}$$

where, the interaction probability corresponding to the $MFP_{(E)}$, is around 0.632.

Regarding the *standard*-sized monolithic cylindrical scintillation crystals, 1×1, 2×2 and 3×3, usually utilized for spectroscopic general-purpose, have been investigated. In addition, also the ones with decreasing heights 2×1, 2×1/2, down to 2×1/16 (around 1.6 mm-thick) used for some high-resolution small-field-of-view medical imaging have been evaluated.

The right-parallelepiped square-base-sized pixels have been also included in this study because of their involvement in PET applications (Casey and Nutt, 1986) and, potentially, in SPECT (Borrazzo *et al*., 2016), as well as in the field of intraoperative probes (Pani *et al*., 2016). Their height has been set at 50 mm for NaI: Tl, essentially for PET.

The results of the V_{ratio} evaluations for these crystals are shown graphically in Fig. 12, where the larger parallelepiped crystals and the smaller ones are referred to as "LR pixels" and "HR pixels", respectively. The Low (spatial) Resolution setups having pixel-base from 3×3- to 6×6-mm^2, by 1-mm steps, are referred to as “LR pixels” in Fig. 12. In addition, the High (spatial) Resolution pixels sized from 1×1- to 2.5×2.5-mm^2, by 0.5-mm side-steps, have been also evaluated as a comparison.

Volumetric-Ratio Results

The trends of the volumetric ratio V_{ratio} as a function of the value of the figure-of-merit *S/V* for the Iodine-K X-rays from NaI are plotted in Fig. 12 for the crystal sizes above described. Two contrasting trends, one descending and the other ascending for the parallelepiped and the cylindrical ones, respectively, are shown in the examined range. The *S/V* ratio parameter seems unsuccessful, in the examined domain, in taking into account the differences in the size, the shape, as well as in the elemental composition of the scintillator itself. Moreover, the parallelepiped crystals (upper curve) show a more marked tendency (10 times about) to advantage X-ray escape in comparison with the cylindrical ones (lower curve).